CBPF-NF-007/00

Cosmic crystallography: the euclidean isometries

A. Bernui*

Facultad de Ciencias, Universidad Nacional de Ingeniería
Apartado 139, Lima 31, Peru

A.F.F. Teixeira*

Departamento de Relatividade e Partículas
Centro Brasileiro de Pesquisas Físicas
22290-180 Rio de Janeiro – RJ, Brasil

Abstract

Exact expressions for probability densities of conjugate pair separation in euclidean isometries are obtained, for the cosmic crys- tallography. These are the theoretical counterparts of the mean histograms arising from computer simulation of the isometries. For completeness, also the isometries with fixed points are examined, as well as the orientation reversing isometries.

1 Introduction

Various methods have been proposed to investigate the shape of the universe, and cosmic crystallography (CC) is one of them [1]. As CC ponders, if the universe is multiply connected (MC) then multiple images of a same cosmic object may be seen in the sky. The separations between these images are correlated by the geometry and the topology of the spacetime; so if one selects a catalog of n observed images of various cosmic objects and performs a histogram of the $n(n-1)/2$ separations between these n images, then the existing correlations must somehow show up.

It was recently examined [2] in what respects the histogram for a multiply connected observed universe should differ from that of a simply connected (SC) one, with same geometry and radius. It was found that each isometry of the MC universe individually imprints either a small localized deformity on the histogram of the SC universe [2], or a sharp spike if the isometry is a Clifford translation [3].

Since each observed universe model has a unique pair separation normalized histogram, a strategy to unveil the cosmic topology seems straightforward: one should compare the histogram obtained from observational astronomy with histograms obtained from computer simulated universe models with prescribed topologies.

Both types of histograms (observational and simulated) are infected with statistical noises, and methods to reduce these noises are desirable. A suggestion was made, to replace the histogram related to the SC component of the simulated model by an *exact* continuous probability density function. For each geometry with constant curvature the corresponding function was then derived [4]; however, appro-

*e-mail: bernui@fc-uni.edu.pe, teixeira@cbpf.br

priate functions were still lacking, to replace the histograms related to each isometry component [5].

In the present study we derive some of these functions, namely the normalized pair separation probability densities for the *euclidean* isometries. Following the prescriptions of ref. [2], if we now merge these new functions with the functions already given in [4] then we obtain noiseless normalized probability densities more suitable for comparing with the normalized observational histograms. For completeness we also examine the euclidean isometries with fixed point, as well as the orientation reversing isometries.

2 The euclidean isometries

The isometries of the euclidean space E^3 are the (pure) translations t, (pure) rotations ω, screw motions $t\omega$, (pure) reflections ϵ, and glide reflections ϵt. While t, ω, and $t\omega$ are orientation preserving, ϵ and ϵt reverse the orientation of E^3; and while t, $t\omega$, and ϵt act freely on E^3, ω and ϵ have fixed points. We study all five isometries for the sake of completeness, although cosmic crystallography is presently interested on the orientation preserving isometries without fixed points, namely t and $t\omega$ only.

Our general approach to investigate an isometry g in cosmic crystallography is first consider a solid ball $\mathcal{B}$ with radius a, then apply g to $\mathcal{B}$ thus producing a new solid ball $\mathcal{B}_g$, next consider the set of points $P \in \mathcal{B}$ whose corresponding transformed points P_g are also in $\mathcal{B}$, finally randomly select a pair $(P,\ P_g)$ and ask for the probability $\mathcal{P}_g^{\mathcal{B}}(l)dl$ that their separation lies between the values l and $l+dl$. The normalization condition

$$\int_0^\infty \mathcal{P}_g^{\mathcal{B}}(l)dl = 1 \qquad (2.1)$$

must be obeyed.

It is clear that the balls $\mathcal{B}$ and $\mathcal{B}_g$ need intersect, so the separation m between their centers C and C_g has to satisfy

$$m < 2a\,. \qquad (2.2)$$

The intersection $\mathcal{B} \cap \mathcal{B}_g$ is a rotationally symmetric solid lens whose diameter, thickness, and volume are (see figure 1)

$$\begin{aligned} D &= \sqrt{4a^2 - m^2}, \\ T &= 2a - m, \\ V_g^{\mathcal{B}} &= \frac{\pi}{12}(2a-m)^2(4a+m)\,. \end{aligned} \qquad (2.3)$$

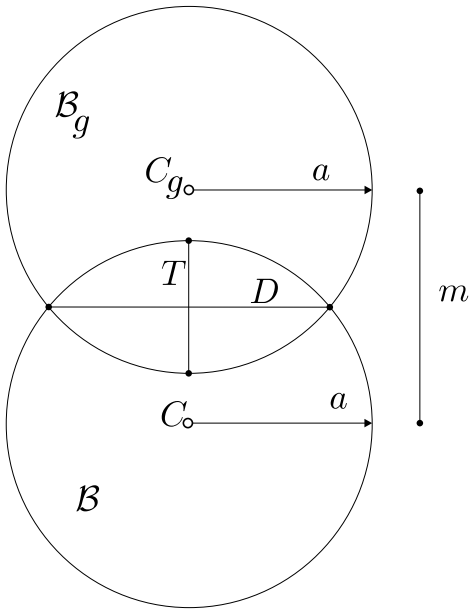

Figure 1 The solid balls $\mathcal{B}$ and $\mathcal{B}_g$ both with radius a intersect in a solid lens with diameter D and thickness T. □

3 Translations, screw motions, and rotations

Translations

If the euclidean space is subjected to a nonzero translation t, the probability density that a point P be displaced a distance l is clearly

$$\mathcal{P}_t(l) = \delta(l-t)\,, \qquad (3.1)$$

the Dirac delta; the density satisfies the normalization condition (2.1), and does not depend on the ball $\mathcal{B}$.

Basics on screw motions of a solid ball

In E^3, imagine a straight line $\mathcal{L}$ placed at a distance b from the center C of the solid ball $\mathcal{B}$ with radius a; $\mathcal{L}$ and $\mathcal{B}$ may intersect ($b < a$), be tangent ($b = a$) or be disjoint ($b > a$); see figure 2.

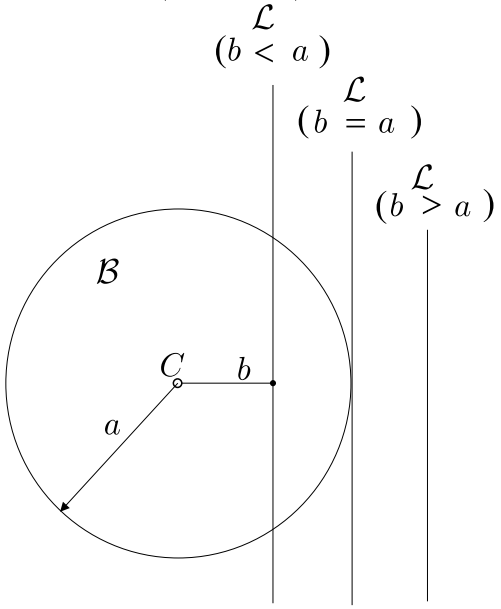

Figure 2 Relative positions of a solid ball $\mathcal{B}$ with radius a and a straight line $\mathcal{L}$ at a distance b from the center of $\mathcal{B}$. □

Now consider a screw motion g of the ball, with nonzero translation t parallel to the line $\mathcal{L}$ and nonzero rotation ω around the line; for our purposes the senses of t and ω are irrelevant, so for definiteness and simplicity we assume $t > 0$ and $0 < \omega \leq \pi$.

The separation m between the centers C and C_g of the intersecting balls $\mathcal{B}$ and $\mathcal{B}_g$ is

$$m = \sqrt{t^2 + 4\,b^2 \sin^2\omega/2}, \qquad (3.2)$$

and the condition $m < 2a$ implies the constraint

$$t^2 + 4\,b^2 \sin^2\omega/2 < 4a^2 \qquad (3.3)$$

between the four independent parameters a, b, t, and ω; see figure 3.

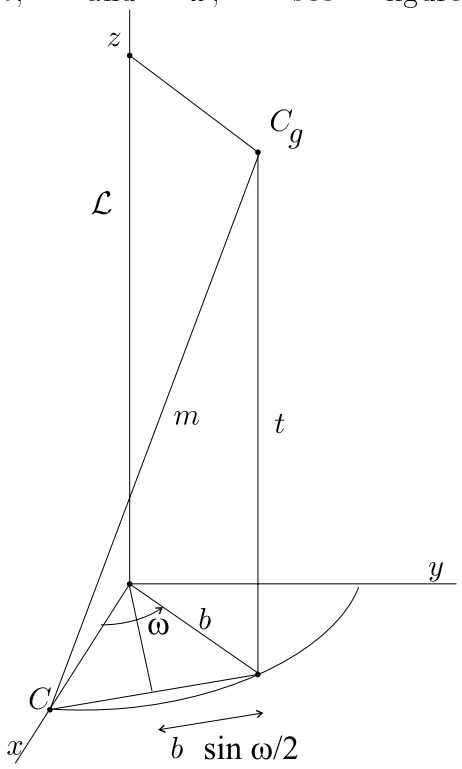

Figure 3 A solid ball (not displayed) with center C rotates ω around the line $\mathcal{L}$ (the z axis) and translates t parallel to the axis, eventually reaching the position centered at C_g; both centers C and C_g are at a distance b from the axis, and their separation m must be smaller than the sum $2a$ of the two radii in order that the balls intersect. □

We next introduce the auxiliary variable r and a function $Q_g^{\mathcal{B}}(r)$ which help simplify our study. Call r the separation between the point P (also P_g) and the axis $\mathcal{L}$ (see figure 4); it is related to l (the separation from P to P_g) through

$$l^2 = t^2 + 4\,r^2 \sin^2\omega/2\ ; \qquad (3.4)$$

for each isometry (t, ω) this is a bijective relation between l and r, so the probability density $\mathcal{P}_g^{\mathcal{B}}(l)$ of finding a g-pair with mutual sep-

aration l parallels the akin probability density $Q_g^{\mathcal{B}}(r)$ of finding a g-pair whose members (both in $\mathcal{B}$) are at a distance r from the axis of the motion:

$$\mathcal{P}_g^{\mathcal{B}}(l)dl = Q_g^{\mathcal{B}}(r)dr. \tag{3.5}$$

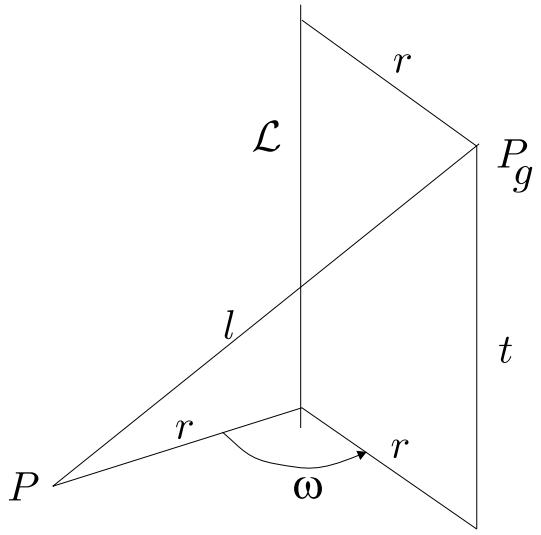

Figure 4 Under the screw motion g with axis $\mathcal{L}$, translation t, and rotation ω, a point P separated r from $\mathcal{L}$ moves to the position P_g at the distance l given by eq. (3.4). □

Clearly the normalization condition

$$\int_0^\infty Q_g^{\mathcal{B}}(r)dr = 1 \tag{3.6}$$

is also to be satisfied. Once we obtain $Q_g^{\mathcal{B}}(r)$, and since from (3.4) we have

$$r = \frac{\sqrt{l^2 - t^2}}{2\sin\omega/2}\ , \tag{3.7}$$

then we will finally compute

$$\mathcal{P}_g^{\mathcal{B}}(l) = \frac{dr}{dl}\,\mathcal{Q}_g^{\mathcal{B}}[r(l)]. \tag{3.8}$$

To obtain $Q_g^{\mathcal{B}}(r)$ we first consider a sufficiently long cylinder $\mathcal{C}_r$ with radius r and axis $\mathcal{L}$. A short reflection gives that the probability density $Q_g^{\mathcal{B}}(r)$ is linearly proportional to the area $S_g^{\mathcal{B}}(r)$ of the intersection $\mathcal{B} \cap \mathcal{B}_g \cap \mathcal{C}_r$; the coefficient of proportionality is the inverse of the volume $V_g^{\mathcal{B}}$ of the intersection $\mathcal{B} \cap \mathcal{B}_g$, eq.(2.3):

$$Q_g^{\mathcal{B}}(r) = \frac{area(\mathcal{B} \cap \mathcal{B}_g \cap \mathcal{C}_r)}{vol(\mathcal{B} \cap \mathcal{B}_g)} = \frac{S_g^{\mathcal{B}}(r)}{V_g^{\mathcal{B}}}. \tag{3.9}$$

To find the area $S_g^{\mathcal{B}}(r)$ we first assume the line $\mathcal{L}$ (the axis of the screw motion) along the cartesian z-axis; the cylinder $\mathcal{C}_r$ with axis $\mathcal{L}$ and radius a then has equation

$$x^2 + y^2 = r^2. \tag{3.10}$$

Still without loss of generality we take the center C of the solid ball $\mathcal{B}$ with radius a at the cartesian position $(b,\ 0,\ 0)$; the points of $\mathcal{B}$ then satisfy

$$(x-b)^2 + y^2 + z^2 \le a^2. \tag{3.11}$$

Finally the center C_g of the solid ball $\mathcal{B}_g$ is at the cartesian position $(b\cos\omega,\ b\sin\omega,\ t)$, so the points of $\mathcal{B}_g$ satisfy

$$\begin{aligned}(x - b\cos\omega)^2 \ &+\ (y - b\sin\omega)^2 \\ &+\ (z-t)^2 \le a^2\,. \end{aligned} \tag{3.12}$$

$S_g^{\mathcal{B}}(r)$ is then the area of the surface whose points (x, y, z) satisfy (3.10), (3.11), and (3.12) simultaneously. To visualize this surface $\mathcal{B} \cap \mathcal{B}_g \cap \mathcal{C}_r$ we first consider the surface $\mathcal{B} \cap \mathcal{C}_r$, then the similar surface $\mathcal{B}_g \cap \mathcal{C}_r$, and finally the *combined* intersection $(\mathcal{B} \cap \mathcal{C}_r) \cap (\mathcal{B}_g \cap \mathcal{C}_r)$.

The form of the intersection $\mathcal{B} \cap \mathcal{C}_r$ depends on the relative values of a, b, and r (see figure 5):
(i) if $0 < r < a - b$ then all generatrices of $\mathcal{C}_r$ penetrate into $\mathcal{B}$: the intersection is a topological ring (an annulus, a compact cylinder, a disc with a hole in it);
(ii) if $|a - b| < r < a + b$ then only a part of the generatrices of $\mathcal{C}_r$ goes through $\mathcal{B}$: the intersection is a topological disc;

(iii) if $a+b<r$, or if $0<r<b-a$, then there is no intersection.

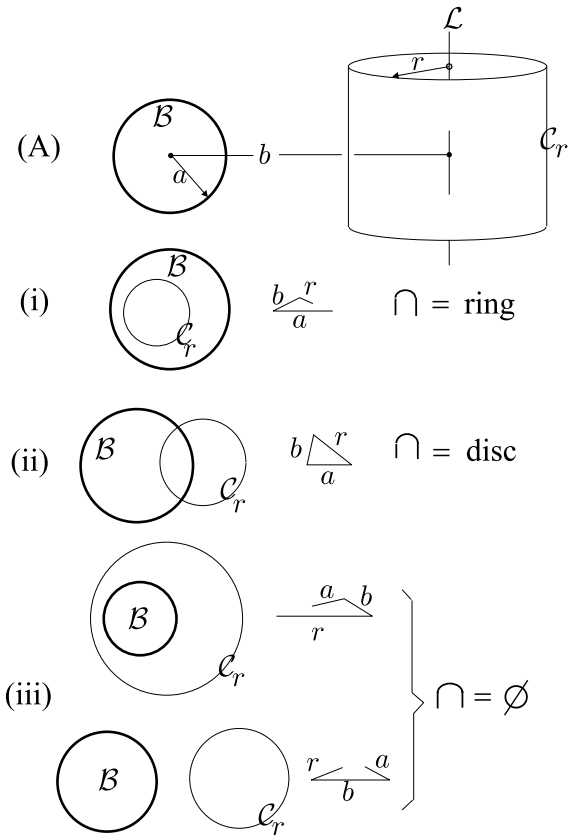

Figure 5 (A) The solid sphere $\mathcal{B}$ and the sufficiently long cylindrical surface $\mathcal{C}_r$, in perspective; in the other drawings the line of sight is the vertical;
(i) the intersection $\mathcal{B}\cap\mathcal{C}_r$ is a topological ring when $0<r<a-b$ (loosely saying, a is too large);
(ii) $\mathcal{B}$ and $\mathcal{C}_r$ intersect in a topological disc when $|a-b|<r<a+b$ (then a, b, and r may form a triangle);
(iii) $\mathcal{B}$ and $\mathcal{C}_r$ do not intersect when $a+b<r$ nor when $0<r<b-a$ (loosely saying, either r or b is too large). □

Since the intersections $\mathcal{B}\cap\mathcal{C}_r$ are drawn on the cylinder $\mathcal{C}_r$ itself, we use the cylindrical coordinates ϕ (the azimuthal angle) and z (altitude) to visualize them. A ring-like intersection $\mathcal{B}\cap\mathcal{C}_r$ is then bounded by the two curves (see figure 6)

$$z=\pm\sqrt{a^2-b^2-r^2+2br\cos\phi}\,, \qquad (3.13)$$

where $\phi\in(-\pi,\pi]$; the positive curve oscillates between the extreme values

$$\begin{aligned} z_{max} &= \sqrt{a^2-(b-r)^2}\,, \\ z_{min} &= \sqrt{a^2-(b+r)^2}\,. \end{aligned} \qquad (3.14)$$

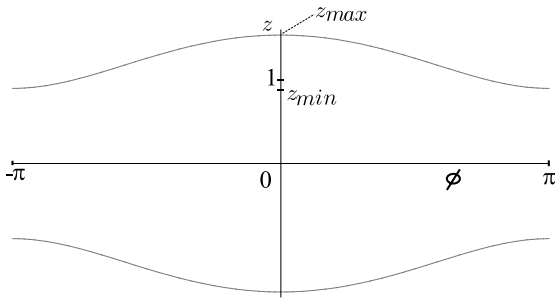

Figure 6 The ring-like intersection $\mathcal{B}\cap\mathcal{C}_r$, eq.(3.13), when $a=4$, $b=19/5$, and $r=1/10$. The boundaries at $\phi=-\pi$ and $\phi=\pi$ are identified. The upper and lower boundaries are not sinusoidal. □

In the disc-like intersection $\mathcal{B}\cap\mathcal{C}_r$ (see figure 7) the surface is again read from (3.13), but now $\phi\in[-\phi_{max},\phi_{max}]$ with

$$\phi_{max}=\cos^{-1}\,\frac{b^2+r^2-a^2}{2br}; \qquad (3.15)$$

while z_{max} is still given in (3.14), $z_{min}=0$ now.

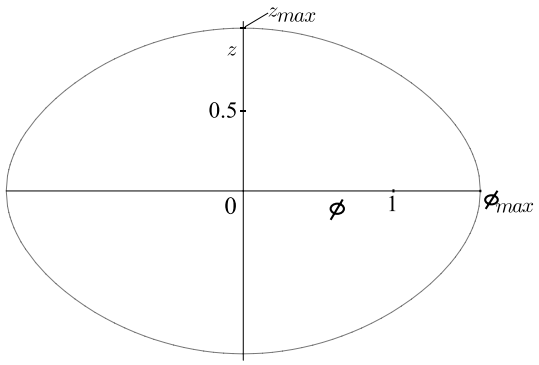

Figure 7 The disc-like intersection $\mathcal{B} \cap \mathcal{C}_r$, eq.(3.13), when $a = 1$ and $b = r = 1/\sqrt{2}$; it is an oval (not an ellipse) centered at $\phi = z = 0$, with $\phi_{max} = \pi/2$ and $z_{max} = 1$. □

A disc-like intersection $\mathcal{B}_g \cap \mathcal{C}_r$ is a g-transported copy of the corresponding intersection $\mathcal{B} \cap \mathcal{C}_r$, parallelly dragged on the cylinder: while $\mathcal{B} \cap \mathcal{C}_r$ is centered at $(\phi = 0, z = 0)$, the center of $\mathcal{B}_g \cap \mathcal{C}_r$ is at $(\phi = \omega, z = t)$.

Similar statements are true for the ring-like intersections $\mathcal{B}_g \cap \mathcal{C}_r$. By inspection it is then easy to visualize the form of the *combined* intersection $\mathcal{B} \cap \mathcal{B}_g \cap \mathcal{C}_r$ in both disc-like and ring-like cases. Since ϕ has a cyclic character, the nonempty intersection of two discs on $\mathcal{C}_r$ can be either 1 or 2 discs, while two rings intersect in either 1 or 2 discs, or 1 ring (see figures 8 and 9).

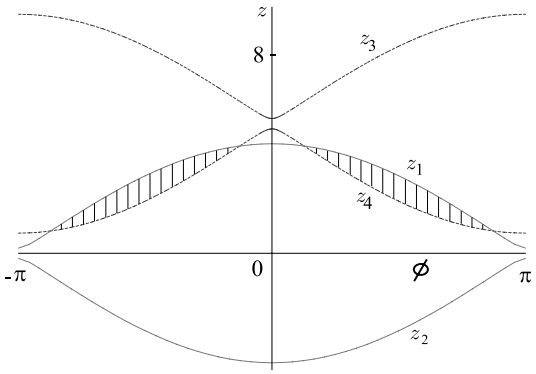

Figure 8 Instance of disconnected intersection $\mathcal{B} \cap \mathcal{B}_g \cap \mathcal{C}_r$ (dashed areas) when $\mathcal{B} \cap \mathcal{C}_r$ (and $\mathcal{B}_g \cap \mathcal{C}_r$) are ring-like; here $a = 4.505$, $b = 2$, $r = 2.5$, $t = 5.3$, and $\omega = \pi$. □

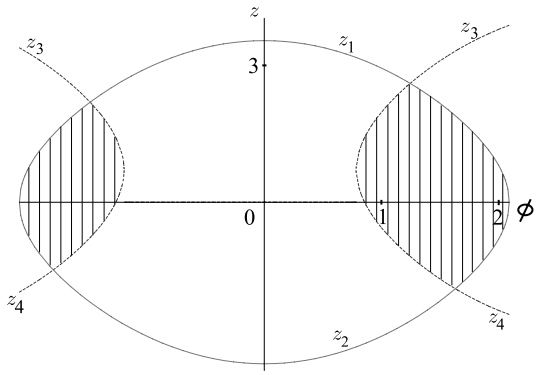

Figure 9 Instance of disconnected intersection $\mathcal{B} \cap \mathcal{B}_g \cap \mathcal{C}_r$ (dashed areas) when $\mathcal{B} \cap \mathcal{C}_r$ (and $\mathcal{B}_g \cap \mathcal{C}_r$) are disc-like; here $a = 3.5$, $b = r = 2$, $t = 0.7$, and $\omega = 14\pi/15$. □

We are now ready to evaluate the area $S_g^{\mathcal{B}}(r)$ of the combined intersection $\mathcal{B} \cap \mathcal{B}_g \cap \mathcal{C}_r$; given the fixed values of a, b, t, and ω, then for each value of r we need to integrate the differential

$$dS_g^{\mathcal{B}}(r) = \Delta z . r d\phi \,, \qquad (3.16)$$

where $\Delta z(r, \phi)$ is the varying height of the intersection, and where the limits of integration in ϕ may vary with r (see eq.(3.15)).

As is evident from figures 8 and 9, the combined intersection is always bounded by one of the two curves

$$z_1(\phi) = \sqrt{a^2 - b^2 - r^2 + 2br\cos\phi} \;, \quad (3.17)$$

$$z_3(\phi) = t + \sqrt{a^2 - b^2 - r^2 + 2br\cos(\phi - \omega)}, \quad (3.18)$$

from the upper side, and one of the two curves

$$z_2(\phi) = -z_1(\phi) \;, \qquad (3.19)$$

$$z_4(\phi) = t - \sqrt{a^2 - b^2 - r^2 + 2br\cos(\phi - \omega)}, \quad (3.20)$$

from the lower side. Further, we only have nonempty combined intersection when

$z_1(\phi) > z_4(\phi)$. We then obtain

$$S_g^{\mathcal{B}}(r) = r \int_{-\phi_{max}}^{\phi_{max}} \Theta(z_1 - z_4) \times \Big[min(z_1, z_3) - max(z_2, z_4) \Big] d\phi \,, \quad (3.21)$$

with ϕ_{max} given by (3.15) for disc-like intersections, and $\phi_{max} = \pi$ for ring-like intersections; Θ is the step function with values 0 and 1.

Elliptic integrals

As is seen from eqs. (3.17)-(3.21), the area $S_g^{\mathcal{B}}(r)$ involves terms of the form

$$A(r) = \int_0^{\alpha(r)} \sqrt{a^2 - b^2 - r^2 + 2br\cos\phi}\, d\phi, \quad (3.22)$$

with $\cos(\phi - \omega)$ sometimes replacing $\cos\phi$ in the integrand. To evaluate these terms we define

$$\begin{aligned} f^2(r) &= a^2 - (b - r)^2 \,, \\ k^2(r) &= \frac{4br}{f^2(r)} \,, \end{aligned} \quad (3.23)$$

after noting that the condition $f^2(r) > 0$ is satisfied by all nonempty intersections $\mathcal{B} \cap \mathcal{C}_r$. Then introduce the (incomplete) elliptic integral of 2^{nd} kind

$$E(\gamma, k) = \int_0^{\gamma} \frac{\sqrt{1 - k^2 x^2}}{\sqrt{1 - x^2}} dx \,, \quad (3.24)$$

and finally have the integral (3.22) expressed as

$$A(r) = 2f(r) E\Big(\sin\frac{1}{2}\alpha(r),\, k(r) \Big) \,, \quad (3.25)$$

where $f = \sqrt{f^2}$ and $k = \sqrt{k^2}$. When $\gamma = 1$ in (3.24), or equivalently $\alpha = \pi$ in (3.22), we have the complete elliptic integral of 2^{nd} kind

$$E(k) = E(1, k) \,; \quad (3.26)$$

the functions $E(k)$ only appear in the ring-like intersections.

Which of z_1 or z_3 is minimum in (3.21), and which of z_2 or z_4 is maximum and whether $z_1 > z_4$ or $z_1 < z_4$, usually depends on the angle ϕ; clearly also the values of the parameters a, b, t, and ω are relevant, well as the radius r.

A sample screw motion with $b \neq 0$

We consider the case with $a = t = 1/\sqrt{2}$, $b = 1/\sqrt{8}$, $\omega = \pi$; the intersection $\mathcal{B} \cap \mathcal{C}_r$ is then ring-like for $0 < r < 1/\sqrt{8}$ (equivalently $1/\sqrt{2} < l < 1$), is disc-like for $1/\sqrt{8} < r < 3/\sqrt{8}$ (or $1 < l < \sqrt{5}$), and is empty for larger values of r and l. The combined intersection $\mathcal{B} \cap \mathcal{B}_g \cap \mathcal{C}_r$ has a ring-like regime for $0 < r < 1/\sqrt{8}$ $(1/\sqrt{2} < l < 1)$, then a two separate discs regime for $1/\sqrt{8} < r < 1/2$ $(1 < l < \sqrt{3/2})$, and is empty for larger r and l.

We first consider the ring-like regime: preliminarly find, from (3.23),

$$\begin{aligned} f^2(r) &= \frac{3}{8} + \frac{r}{\sqrt{2}} - r^2 \,, \\ k^2(r) &= \frac{\sqrt{2}\, r}{f^2} \,, \end{aligned} \quad (3.27)$$

and the area (3.21) of the intersection $\mathcal{B} \cap \mathcal{B}_g \cap \mathcal{C}_r$,

$$S_g^{\mathcal{B}}(r) = r\Big(8\, f\, E(k) - \pi\sqrt{2} \Big) \;; \quad (3.28)$$

now since

$$r = \frac{1}{2}\sqrt{l^2 - 1/2} \,, dr/dl = l/(4r) \,, \quad (3.29)$$

the probability density (3.8) is, for $1/\sqrt{2} < l < 1$,

$$\mathcal{P}_g^{\mathcal{B}}(l) = \frac{l}{4V_g^{\mathcal{B}}} \Big(8\, f\, E(k) - \pi\sqrt{2} \Big) \,, \quad (3.30)$$

where the volume of $\mathcal{B} \cap \mathcal{B}_g$ is

$$V_g^{\mathcal{B}} = \pi(4\sqrt{2} - 5)/12 \,. \quad (3.31)$$

Clearly $f(r)$ and $k(r)$ in (3.30) need consider the dependence $r(l)$ given in (3.29).

To describe the two-discs regime we further define

$$\begin{aligned} g(r) &= \sqrt{1/(2r)^2 - 1}\,, \\ g_\pm(r) &= \sqrt{\frac{1 \pm g}{2}}\,, \end{aligned} \tag{3.32}$$

then obtain for the area (3.21)

$$\begin{aligned} S_g^{\mathcal{B}}(r) &= 8\,r\,f\,\Big(E(g_+,k) - E(g_-,k)\Big) \\ &+ \sqrt{2}r(2\cos^{-1}g - \pi)\,, \end{aligned} \tag{3.33}$$

and finally, for $1 < l < \sqrt{3/2}$, the probability density

$$\begin{aligned} \mathcal{P}_g^{\mathcal{B}}(l) &= \frac{l}{4V_g^{\mathcal{B}}}\Big[8f\Big(E(g_+,k) - E(g_-,k)\Big) \\ &+ \sqrt{2}\,(2\cos^{-1}g - \pi)\Big]\,. \end{aligned} \tag{3.34}$$

In (3.34) we clearly need replace r by its value $r(l)$ in (3.29) in the functions f, g, g_+, g_-, and k. In figure 10 we reproduce the function $\mathcal{P}_g^{\mathcal{B}}(l)$ for this sample screw motion, for the whole interval $1/\sqrt{2} < l < \sqrt{3/2}$.

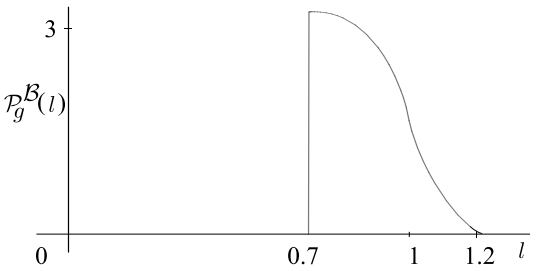

Figure 10 The probability density $\mathcal{P}_g^{\mathcal{B}}(l)$ for the screw motion of the solid ball $\mathcal{B}$ with $a = 2b = t = 1/\sqrt{2}$, and $\omega = \pi$. For $l \in [1/\sqrt{2}\,, 1]$ we use the ring-like equation (3.30), while for $l \in [1\,, \sqrt{3/2}]$ the two-discs equation (3.34) is used. The integrated area is 1. □

The special cases with $b = 0$

In these cases the axis $\mathcal{L}$ of the screw motion contains the centers C and C_g of the solid balls $\mathcal{B}$ and $\mathcal{B}_g$; the intersections $\mathcal{B} \cap \mathcal{C}_r$ and $\mathcal{B}_g \cap \mathcal{C}_r$ are ring-like and have constant width, as well as the combined intersections $\mathcal{B} \cap \mathcal{B}_g \cap \mathcal{C}_r$. From (3.2) we have $m = t$, then (2.3) gives

$$V_g^{\mathcal{B}} = \frac{\pi}{12}(2a - t)^2(4a + t) \qquad [b = 0] \tag{3.35}$$

provided $t < 2a$; this sine qua non is assumed whenever $b = 0$. The equations (3.17)-(3.20) simplify to

$$\begin{aligned} z_1 = -z_2 &= \sqrt{a^2 - r^2}\,, \\ z_3 &= t + z_1\,, z_4 = t - z_1\,, \end{aligned} \tag{3.36}$$

provided $r < a$; since we assumed $t > 0$, we have $min(z_1, z_3) = \sqrt{a^2 - r^2}$ and $max(z_2, z_4) = t - \sqrt{a^2 - r^2}$, while the condition $z_1 > z_4$ implies

$$r < r_{max} = \sqrt{a^2 - t^2/4}\,. \tag{3.37}$$

The area of the combined intersection is then

$$S_g^{\mathcal{B}}(r) = 2\pi r(2\sqrt{a^2 - r^2} - t) \quad [b = 0] \tag{3.38}$$

whenever positive, otherwise it is zero. Finally the probability density is, when $b = 0$,

$$\begin{aligned} \mathcal{P}_g^{\mathcal{B}}(l) &= \frac{dr}{dl}\frac{S_g^{\mathcal{B}}(r)}{V_g^{\mathcal{B}}} \\ &= \frac{6\,l\,(2\sqrt{a^2 - r^2} - t)}{(2a - t)^2(4a + t)}\,\csc^2\omega/2 \end{aligned} \tag{3.39}$$

if positive, otherwise it is zero; in (3.39) one clearly has to substitute r for its expression eq.(3.7). As a matter of fact we have $\mathcal{P}_g^{\mathcal{B}}(l) \neq 0$ when $b = 0$ only for $l_{min} < l < l_{max}$, where

$$\begin{aligned} l_{min} &= t\,, \\ l_{max} &= \sqrt{t^2\cos^2\omega/2 + 4a^2\sin^2\omega/2}\,, \end{aligned} \tag{3.40}$$

and we have in these extreme limits

$$\begin{aligned} &\mathcal{P}_g^{\mathcal{B}}(l_{min}) = 6t(2a - t)^{-1}(4a + t)^{-1}\csc^2\omega/2\,, \\ &\mathcal{P}_g^{\mathcal{B}}(l_{max}) = 0\,; \end{aligned} \tag{3.41}$$

a sample graph of $\mathcal{P}_g^{\mathcal{B}}(l)$ for screw motions with $b = 0$ is given in figure 11.

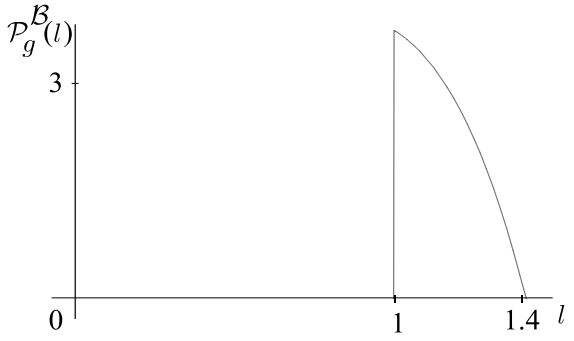

Figure 11 The probability density $\mathcal{P}_g^{\mathcal{B}}(l)$ for the screw motion of the solid ball $\mathcal{B}$ with $b = 0$, $a = 1/\sqrt{2}$, $t = 1$, and $\omega = \pi$, eq.(3.39). The integrated area is 1. Note that $l_{min} = 1$, $l_{max} = \sqrt{2}$, and $\mathcal{P}_g^{\mathcal{B}}(1) = 6(3+\sqrt{2})/7 \sim 3.8$. □

Rotations

A rotation is the limit of a screw motion when the translation tends to zero, so it is formally described by simply setting $t = 0$ in the appropriate preceding equations. In particular, eq. (3.4) becomes $l = 2r\sin\omega/2$. Rotations of the solid sphere $\mathcal{B}$ are classified into two categories:

(i) if $a < b$ then $\mathcal{B}$ is exempt of fixed points;

(ii) if $b < a$ then the axis $\mathcal{L}$ traverses $\mathcal{B}$, which has fixed points.

In category $a < b$ the intersection condition (3.3) clearly must be satisfied (see figure 12),

$$b\,\sin\omega/2 < a\ . \tag{3.42}$$

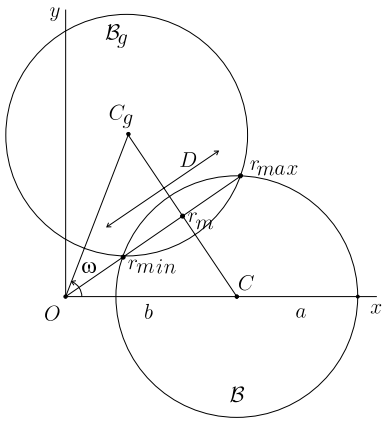

Figure 12 The solid lens $\mathcal{B} \cap \mathcal{B}_g$ when the solid ball $\mathcal{B}$ rotates ω around the z-axis and $b\sin\omega/2 < a < b$; the lens lays between the radial positions r_{min} and r_{max} given by eq. (3.43). □

The lens $\mathcal{B} \cap \mathcal{B}_g$ lays between the radial positions

$$r_{min} = r_m - D/2\,,\ \ r_{max} = r_m + D/2\,,$$
$$r_m = b\,\cos\omega/2\,, \tag{3.43}$$

where r_m is the radial coordinate of the center of the lens and D is its diameter (2.3) with

$$m = 2\,b\,\sin\omega/2\ . \tag{3.44}$$

All intersections $\mathcal{B} \cap \mathcal{C}_r$ (and $\mathcal{B}_g \cap \mathcal{C}_r$) are topological discs. Since $z_1 > z_4$ and $z_4 = -z_3$ in rotations, the area (3.21) has the simpler expression

$$S_g^{\mathcal{B}}(r) = 2r\int_{-\phi_{max}}^{\phi_{max}} min(z_1, z_3)d\phi\ . \tag{3.45}$$

When $b\,\sin\omega/2 < a < b$ and $r_m - D/2 < r < r_m + D/2$ we obtain

$$S_g^{\mathcal{B}}(r) = 8rf\Big[E(1/k,k) - E(\sin\omega/4,k)\Big]\,, \tag{3.46}$$

with $f(r)$ and $k(r)$ given in (3.23). The probability density (3.8) is easily written if we take in succession $l = 2r\sin\omega/2$, then $Q_g^{\mathcal{B}}(r) = S_g^{\mathcal{B}}(r)/V_g^{\mathcal{B}}$ with (3.46), finally $V_g^{\mathcal{B}}$ in (2.3) with

$m = 2\,b\,\sin\omega/2$; in figure 13 a sample graph of $\mathcal{P}_g^{\mathcal{B}}(l)$ for rotation with $a < b$ is given.

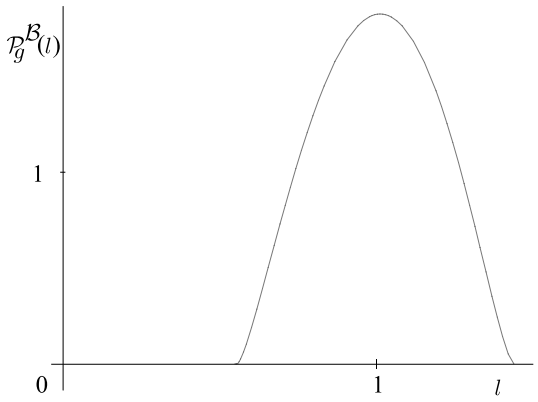

Figure 13 The probability density $\mathcal{P}_g^{\mathcal{B}}(l)$ for a rotation ω of the solid ball $\mathcal{B}$ with radius $a < b$. Here $a = 1\,, b = 2\,,$ and $\omega = \pi/6$. The integrated area is 1. □

In category $b < a$ the intersections $\mathcal{B} \cap \mathcal{C}_r$ are either ring-like or disc-like, and the combined intersections $\mathcal{B} \cap \mathcal{B}_g \cap \mathcal{C}_r$ can be of three types according to the relative values of $a, b, \omega,$ and r (see figure 14):

(i) a ring, when $0 < r < a - b$; then

$$S_g^{\mathcal{B}}(r) = 8rf\,\Big[\,2\,E(k) - E(\sin\omega/4,\,k) - E(\cos\omega/4,\,k)\,\Big]\,; \quad (3.47)$$

(ii) a pair of discs, when $a - b < r < D/2 - r_m$; then

$$S_g^{\mathcal{B}}(r) = 8rf\,\Big[\,2\,E(1/k,\,k) - E(\sin\omega/4,\,k) - E(\cos\omega/4,\,k)\,\Big]\,; \quad (3.48)$$

(iii) a disc, when $D/2 - r_m < r < D/2 + r_m$; then

$$S_g^{\mathcal{B}}(r) = 8rf\Big[E(1/k,k) - E(\sin\omega/4,k)\Big]. \quad (3.49)$$

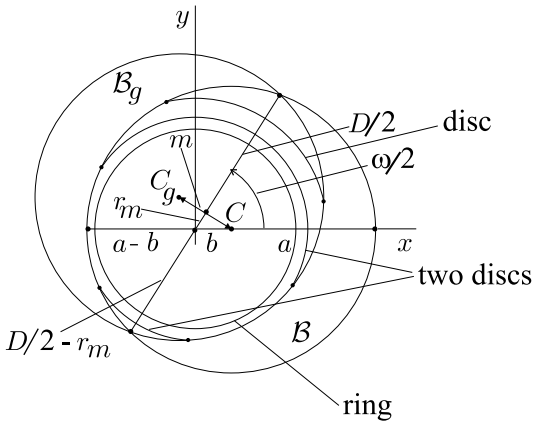

Figure 14 The solid ball $\mathcal{B}$ with center C and radius $a > b$ rotates ω around the z-axis and gives the new ball $\mathcal{B}_g$ with center C_g. The solid lens $\mathcal{B} \cap \mathcal{B}_g$ is intersected by the cylindrical surface $\mathcal{C}_r$ with radius r and axis along the z-axis. The intersection $\mathcal{B} \cap \mathcal{B}_g \cap \mathcal{C}_r$ is a ring if r is small ($0 \le r < a - b$), is a pair of discs for $a - b < r < D/2 - r_m$, and is a single disc when r is larger ($D/2 - r_m < r < D/2 + r_m$). □

In figures 15 and 16 sample graphs of the probability $\mathcal{P}_g^{\mathcal{B}}(l)$ for rotation with $b < a$ are given, for the entire interval $0 < r < D/2 + r_m$.

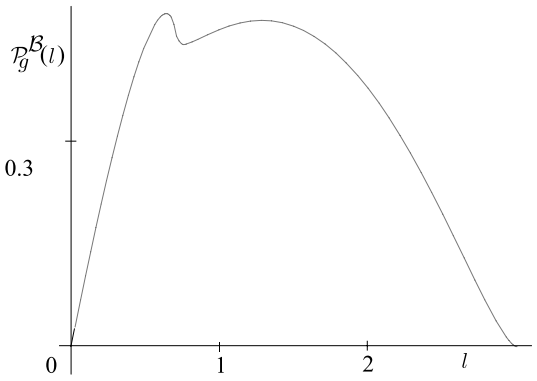

Figure 15 The probability density $\mathcal{P}_g^{\mathcal{B}}(l)$ for a (pure) rotation of the solid ball $\mathcal{B}$ with radius $a > b$. Here $a = 2\,, b = 1.3\,,$ and $\omega = \pi/3$. The integrated area is 1. □

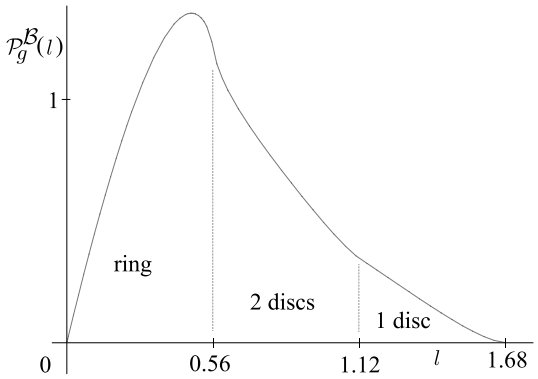

Figure 16 The probability density $\mathcal{P}_g^{\mathcal{B}}(l)$ for a (pure) rotation of the solid ball $\mathcal{B}$ with radius $a > b$. Here $a = 1$, $b = 5/7$, and $\omega = 2\sec^{-1}5$. The region where each of the three expressions (3.47)-(3.49) for $S_g^{\mathcal{B}}(r)$ is used is indicated. The integrated area is 1. □

Rotations with $b = 0$

In the category $b < a$ the special cases $b = 0$ deserve a few words. The solid spheres $\mathcal{B}$ and $\mathcal{B}_g$ coincide, and we easily find that

$$l = 2r\sin\omega/2\,,\quad S_g^{\mathcal{B}}(r) = 4\pi r\sqrt{a^2 - r^2}\,,$$
$$V_g^{\mathcal{B}} = 4\pi a^3/3\,. \tag{3.50}$$

The probability density is then

$$\mathcal{P}_g^{\mathcal{B}}(l) = \frac{3}{8}\frac{l\sqrt{4a^2\sin^2\omega/2 - l^2}}{a^3\sin^3\omega/2} \tag{3.51}$$

whenever $0 \le l \le 2a\sin\omega/2$; a sample graph is given in figure 17.

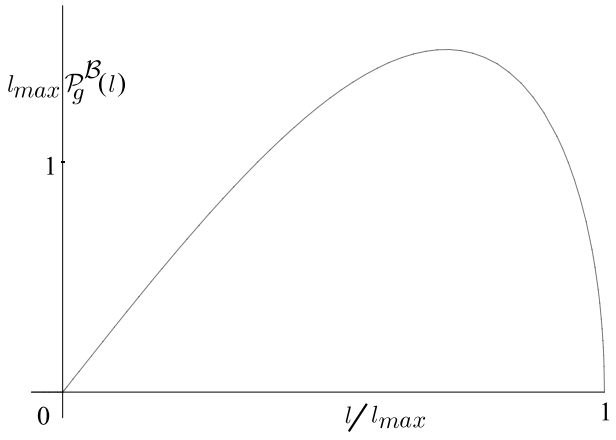

Figure 17 The probability density $\mathcal{P}_g^{\mathcal{B}}(l)$ for a (pure) rotation with $b = 0$. Here $a = 1$, and $\omega = \pi/6$. The integrated area is 1. □

4 Reflections and glide reflections

In E^3, let a solid ball $\mathcal{B}$ with radius a have its center C at the cartesian position $(b, 0, 0)$. Next consider a glide reflection g on the plane $x = 0$ (the plane $\mathcal{X}_0$) with nonzero translation t in the direction $+z$. The center C_g of the glide reflected ball $\mathcal{B}_g$ is at the cartesian position $(-b, 0, t)$, and the separation m between C and C_g is

$$m = \sqrt{4b^2 + t^2}\,. \tag{4.1}$$

The condition of intersection $\mathcal{B} \cap \mathcal{B}_g \neq \phi$ implies the constraint

$$4b^2 + t^2 < 4a^2 \tag{4.2}$$

between the three independent parameters a, b, and t; a fortiori $b < a$, so both balls intersect the plane $\mathcal{X}_0$; see figure 18.

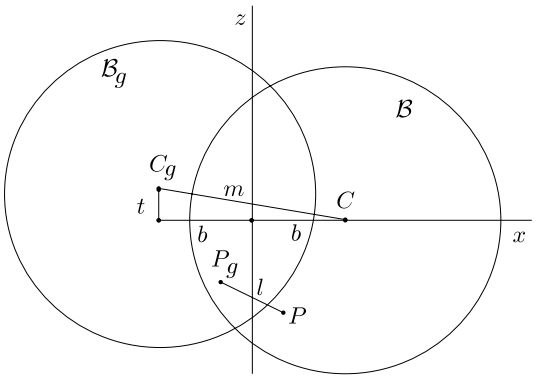

Figure 18 The solid ball $\mathcal{B}$ with center C and radius a is first reflected on the plane $x = 0$ a distance $b < a$ apart, then translated t upwards. □

Now randomly choose a point $P = (x, y, z)$ of $\mathcal{B}$, such that $P_g = (-x, y, z + t)$ is also in $\mathcal{B}$; clearly $P \in \mathcal{B} \cap \mathcal{B}_g$. l being the separation from

P to P_g, we ask for the probability density $\mathcal{P}_g^{\mathcal{B}}(l)$ as described in sec. 2; we readily find

$$\mathcal{P}_g^{\mathcal{B}}(l) = 2\,\frac{area(\mathcal{B}\cap\mathcal{B}_g\cap\mathcal{X}_x)}{vol(\mathcal{B}\cap\mathcal{B}_g)} = 2\,\frac{S_g^{\mathcal{B}}(x)}{V_g^{\mathcal{B}}}\,, \qquad (4.3)$$

where $\mathcal{X}_x$ is one of the two planes

$$x = \pm\frac{1}{2}\sqrt{l^2-t^2}\,; \qquad (4.4)$$

the multiplying factor 2 in (4.3) accounts for these two possibilities, and the volume $V_g^{\mathcal{B}}$ is given in (2.3).

The intersections $\mathcal{B}\cap\mathcal{B}_g\cap\mathcal{X}_x$ are of two types, depending on whether or not the plane $\mathcal{X}_x$ intersects the equator $\mathcal{E}$ of the lens $\mathcal{B}\cap\mathcal{B}_g$ (see figure 19):

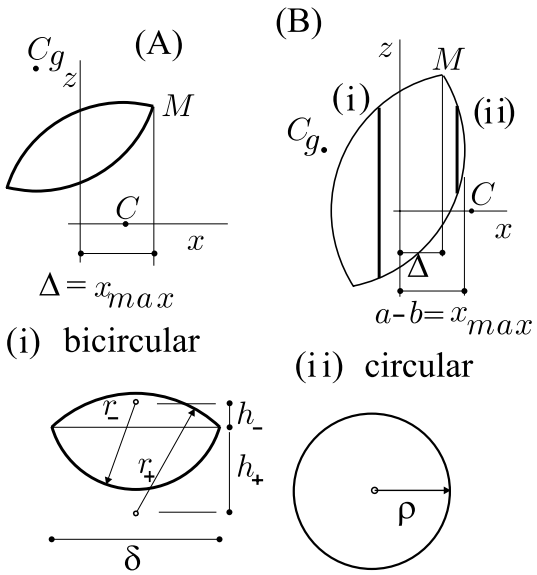

Figure 19 The solid lens $\mathcal{B}\cap\mathcal{B}_g$ and the two types of intersections $\mathcal{B}\cap\mathcal{B}_g\cap\mathcal{X}_x$ when the isometry is a glide reflection. In the equator $\mathcal{E}$ of the lens, M is the point placed farthest from the reflector plane $x=0$. In (**A**), M is below the center C_g of the glide reflected ball $\mathcal{B}_g$, then $x_{max}=x_M=\Delta$ given in (4.8); only bicircular sections (i) are possible. In (**B**), M is above C_g, then $x_{max}=a-b>x_M$ and two types of vertical cross-sections can occur: (i) bicircular, and (ii) circular. □

(i) a bicircular disc, when $\mathcal{X}_x\cap\mathcal{E}\neq\phi$; the disc is enclosed by two circles with unequal radii

$$r_\pm(x) = \sqrt{a^2-(b\mp x)^2}\,. \qquad (4.5)$$

It has area

$$S_g^{\mathcal{B}}(x) = r_-^2\cos^{-1}\frac{h_-}{r_-} + r_+^2\cos^{-1}\frac{h_+}{r_+} - \frac{t\delta}{2}, \qquad (4.6)$$

whenever $|x|<\Delta$, where

$$h_\pm(x) = t/2 \pm 2\,b\,x/\,t\,, \qquad (4.7)$$

$$\Delta = \frac{t}{2}\sqrt{\frac{a^2}{b^2+t^2/4}-1}\,,$$
$$\delta(x) = 2\sqrt{(1+4b^2/t^2)(\Delta^2-x^2)}\,. \qquad (4.8)$$

(ii) a circular disc with radius

$$\rho = \sqrt{a^2+(b+|x|)^2}\,, \qquad (4.9)$$

which appears only when

$$q = 4b(a-b)-t^2>0,\ \ \Delta<|x|<a-b\,; \qquad (4.10)$$

the area of the disc is clearly $\pi\rho^2$.

Collecting together preceding terms we finally obtain

$$\mathcal{P}_g^{\mathcal{B}}(l) = \frac{l}{\sqrt{l^2-t^2}}\frac{1}{V_g^{\mathcal{B}}}\Big[\Theta(\Delta-|x|)\,S_g^{\mathcal{B}}(x) + \Theta(q)\Theta(|x|-\Delta)\Theta(a-b-|x|)\pi\rho^2\Big]\,, \qquad (4.11)$$

valid for $t<l\le l_{max}$ where

$$l_{max} = \sqrt{t^2+4(a-b)^2}\,\Theta(q) + \frac{at}{\sqrt{b^2+t^2/4}}\,\Theta(-q)\,. \qquad (4.12)$$

A graph of $\mathcal{P}_g^{\mathcal{B}}(l)$ is given in figure 20.

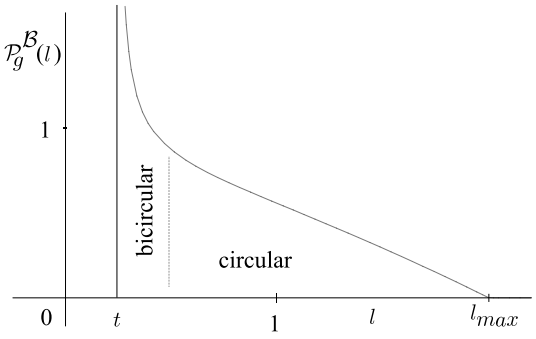

Figure 20 The probability density $\mathcal{P}_g^{\mathcal{B}}(l)$ for a solid ball under a glide reflection, eq.(4.11). Here $a = 2\,, b = 1\,,$ and $t = 0.25\,.$ The regions where the sections $\mathcal{B} \cap \mathcal{B}_g \cap \mathcal{X}_x$ are bicircular or circular are displayed. The function diverges when $l \to t\,,$ nevertheless the integrated area from t to l_{max} is finite. □

Reflections

(Pure) reflections are glide reflections whose translation is $t = 0\,.$

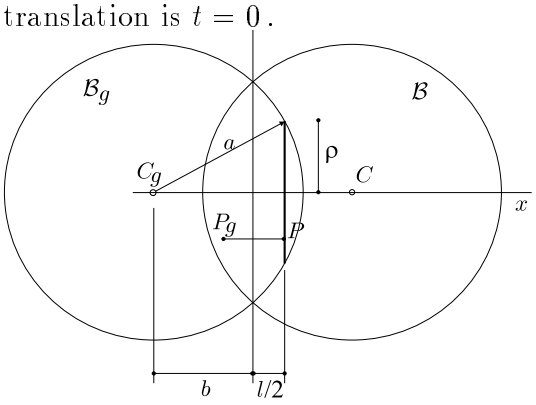

Figure 21 The solid lens $\mathcal{B} \cap \mathcal{B}_g$ when the isometry g is a (pure) reflection on the plane $x = 0\,.$ The sections $\mathcal{B} \cap \mathcal{B}_g \cap \mathcal{X}_x$ are circles with variable radius $\rho\,.$ □

As is evident from figure 21, the probability density $\mathcal{P}_g^{\mathcal{B}}(l)$ is proportional to the area of a disc with radius

$$\rho = \sqrt{a^2 - (b + l/2)^2}\,, \qquad (4.13)$$

and is given by

$$\mathcal{P}_g^{\mathcal{B}}(l) = \frac{3}{2}\frac{a^2 - (b + l/2)^2}{(a - b)^2(2a + b)}\,, \qquad (4.14)$$

for $0 \leq l \leq 2(a - b)$. A graph is presented in figure 22.

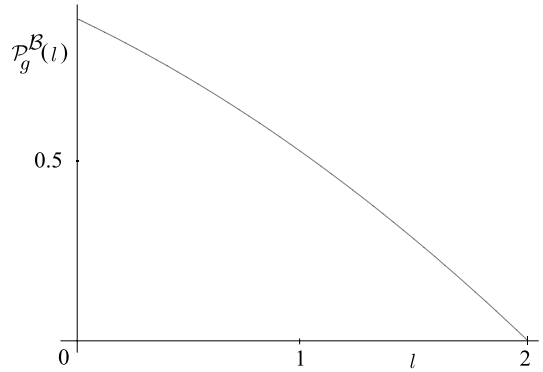

Figure 22 The probability density $\mathcal{P}_g^{\mathcal{B}}(l)$ for a solid ball when the isometry g is a (pure) reflection, eq.(4.14). Here $a = 2$ and $b = 1\,.$ The integrated area is 1. □

5 Discussions

We initially aimed to write out one single expression for the probability density $\mathcal{P}_g^{\mathcal{B}}(l)$ for screw motions of solid balls, valid for whatever values of the *four* parameters $a, b, t\,,$ and ω. However, we soon found that such expression would demand a quite large number of step functions to account for all sort of possibilities. Since in practice the isometries are dealt with one at each time, we found more appropriate to present a simple method to have the exact $\mathcal{P}_g^{\mathcal{B}}(l)$ for each individual screw motion with *fixed* values of the four parameters. Nevertheless, for those isometric motions of solid balls described by *three* or less free parameters the exact expression for $\mathcal{P}_g^{\mathcal{B}}(l)$ for *any* euclidean isometry is short enough and was displayed.

As promised in the Introduction, we exhibited the analytic counterpart $\mathcal{P}_g^{\mathcal{B}}(l)$ of the computer simulations of pair separations histograms of the euclidean isometries in cosmic

crystallography thus far obtained in the literature. The graph of $\mathcal{P}_g^{\mathcal{B}}(l)$ in figure 10 corresponds to the isometries b and c in the Fagundes and Gausmann [6] study, or equivalently the isometries β and δ in Gomero [7]. The discontinuity in $l \sim 0.7$ is not observed in the two upper figures 1 (Universe E4) of [6] due to the strong statistical noise present in these histograms; nevertheless it is clearly seen in the position $s = l^2 = 0.5$ in the *mean* histogram 5b of [3] as well as in the position $l \sim 0.7$ in the mean histograms 1a, 1b, 2b, 4a, and 5 of [5]. Similarly, figure 11 corresponds to the isometry a of [6] and α in [7] and [3]; the discontinuity in $l = 1$ has their counterparts again in the histogram 5b of [3] and in the histograms 1a, 1b, 2a, 4a, and 5 of [5].

In contrast with the screw motions (figures 10 and 11), the pure rotations (figures 13, 15, and 16, all with $t = 0$) do not show discontinuity of $\mathcal{P}_g^{\mathcal{B}}(l)$. Oppositely to figure 13, where $a < b$, figures 15 and 16 correspond to $a > b$, so the ball $\mathcal{B}$ now has fixed points and the graph of $\mathcal{P}_g^{\mathcal{B}}(l)$ effectively starts from $l = 0$. The strange-looking graph in figure 15 was confirmed in a computer simulation; the irregular behavior near $l = 0.7$ corresponds to the narrow r-interval where the pair-of-discs combined intersection eq.(3.48) occurs.

In figure 16 we have chosen values for a, b, and ω such that the three types of combined intersection (ring, pair of discs, and one disc) have equal range in the l scale. *En passant*, the pair-of-discs $l-$range is now wide, and does not originate a bump as did in figure 15.

Figure 17 corresponds to rotation of the solid ball $\mathcal{B}$ around a diameter $\mathcal{D}$; from (3.51) we find that defining $l_{max} = 2a \sin\omega/2$ then the graph of $l_{max}\mathcal{P}_g^{\mathcal{B}}(l)$ against l/l_{max} does not depend on l_{max}. The points of $\mathcal{B}$ along the diameter $\mathcal{D}$ are fixed under the isometry, so the graph again effectively starts from the origin.

Figure 20 corresponds to a glide reflection whose sections $x = const$ in the intersection $\mathcal{B} \cap \mathcal{B}_g$ are either bicircular discs (for small $|x|$) or circular (for larger $|x|$). The minimum displacement l occurs for the points of $\mathcal{B}$ in the intersection with the reflector plane $x = 0$, giving $l_{min} = t$, the translation. Since for all points near the reflector plane we have $l \sim t(1+2|x|^2)$, then these points are displaced almost the same value $l \sim t$; as a consequence, $\mathcal{P}_g^{\mathcal{B}}(l)$ diverges in the vicinity of $l = t$. Nevertheless the integrated area is finite, with value 1.

Between $l = t = 0.25$ and $l \sim 0.5$ we have bicircular sections (4.6), while for $0.5 < l < l_{max} \sim 2.0$ the sections $\mathcal{B} \cap \mathcal{B}_g \cap \mathcal{X}_x$ are circles.

The transition from a glide reflection to a (pure) reflection is worth describing: if in figure 20 we continuously displace the vertical line $l = t = 0.25$ towards $l = 0$, then the region of divergence of $\mathcal{P}_g^{\mathcal{B}}(l)$ shrinks continuously and disappears when $l = 0$, eventually giving the graph of figure 22.

References

[1] R. Lehoucq, M. Lachièze-Rey, and J.-P. Luminet, *Astron. Astroph.* **313**, 339-346 (1996).

[2] G.I. Gomero, A.F.F. Teixeira, M.J. Rebouças and A. Bernui, *Spikes in cosmic crystallography*, gr-qc/9811038 (1998).

[3] G.I. Gomero, M.J. Rebouças and A.F.F. Teixeira, *Spikes in cosmic crystallography II: topological signature of compact flat universes*, gr-qc/9909078 (1999).

[4] A. Bernui and A.F.F. Teixeira, *Cosmic crystallography: three multipurpose functions*, astro-ph/9904180 (1999).

[5] G.I. Gomero, M.J. Rebouças and A.F.F. Teixeira, *A topological signature in cosmic topology*, gr-qc/9911049 (1999).

[6] H.V. Fagundes and E. Gausmann, *Phys. Letters A* **238**, 235-238 (1998).

[7] G. Gomero, *Fundamental polyhedron and glueing data for the sixth euclidean compact orientable 3-manifold*, preprint CBPF-NF-049/97 (1997).